
Neural Splines: Fitting 3D Surfaces with Infinitely-Wide Neural Networks

Francis Williams

Matthew Trager

Joan Bruna

Denis Zorin

New York University

Abstract

We present Neural Splines, a technique for 3D surface reconstruction that is based on random feature kernels arising from infinitely-wide shallow ReLU networks. Our method achieves state-of-the-art results, outperforming Screened Poisson Surface Reconstruction and modern neural network based techniques. Because our approach is based on a simple kernel formulation, it is fast to run and easy to analyze. We provide explicit analytical expressions for our kernel and argue that our formulation can be seen as a generalization of cubic spline interpolation to higher dimensions. In particular, the RKHS norm associated with our kernel biases toward smooth interpolants. Finally, we formulate Screened Poisson Surface Reconstruction as a kernel method and derive an analytic expression for its norm in the corresponding RKHS.

1 Introduction

Estimating a 3D surface from a scattered point-cloud is a classical and important problem in computer vision and graphics. In this task, the input is a set of 3D points sampled from an unknown surface and, possibly, normals of the surface at those points. The goal is to estimate a discrete representation of the surface, for example, a polygonal mesh or an implicit function from the input. This problem is very challenging for several reasons. First, it is inherently ill-posed, since an infinite number of surfaces can interpolate the data. Second, the input 3D points are often incomplete and noisy, as they are acquired from range sensors such as LIDAR, structured light, and laser scans. Ideally, the recovered surface should not interpolate noise but preserve key features and details of the surface.

The most widely used method for surface reconstruction is *Screened Poisson Surface Reconstruction* [20], which solves a screened Poisson equation to find an implicit function whose zero-level set produces an approximating surface. More recently, many papers have used neural networks to represent an implicit function or a local chart in a manifold atlas [29, 12, 15, 3, 13] as a means of reconstructing a surface. These methods can be integrated into a data-driven learning pipeline or directly applied in the so called “overfitting” regime, where a massively overparameterized (*i.e.*, more parameters than input points) neural network is fitted to a single input point cloud as a functional representation for a surface. Empirical evidence has shown that these methods enjoy some form of “implicit regularization” that biases the recovered surface towards smoothness. Moreover, employing early stopping in gradient descent can prevent these approaches from interpolating noise in the data.

Under certain parameter initializations, infinitely-wide neural networks *de facto* behave as kernel machines [19, 9], defining Reproducing Kernel Hilbert Spaces (RKHS), whose kernel is an expectation over neural network features. While providing a simple explanation for the successful optimization of overparametrized models, this regime cannot explain the good generalization properties observed in high-dimensional problems, owing to the inability of such RKHS to approximate non-smooth functions [4]. However, the situation for low-dimensional problems such as surface reconstruction is different, and RKHS can provide powerful characterizations of regularity. In this context, [30] shows that in the univariate case the RKHS norm associated with a wide ReLU network is a weighted

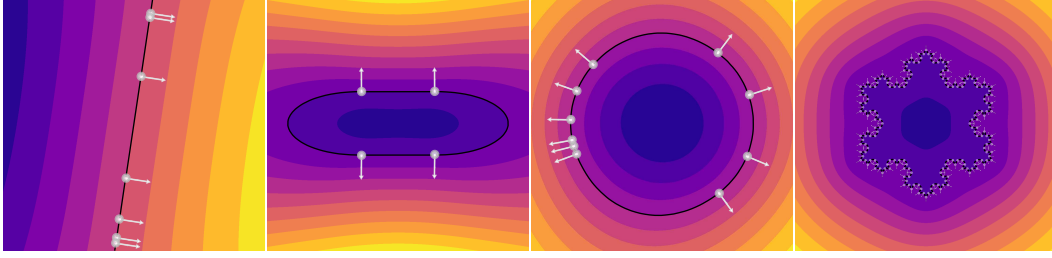


Figure 1: Neural Splines use points (the white dots) and normals (the white arrows) as input and estimate a scalar function whose zero level set (the black lines) corresponds to the reconstructed surface and whose gradient agrees with the normals.

curvature, and leads to cubic spline interpolants. In higher dimensions, similar (albeit more complex) characterizations of the RKHS norm exist [24] (see also Proposition 2).

In this work, we demonstrate, perhaps surprisingly, that kernels arising from shallow ReLU networks are in fact extremely competitive for 3D surface reconstruction, achieving state-of-the-art results and outperforming classical methods as well as non-linear methods based on far more complex neural network optimization. Kernels provide many advantages over neural networks in our context: *(i)* They are well understood theoretically. *(ii)* Kernel regression boils down to solving a linear system, avoiding gradient descent that suffers from slow convergence. *(iii)* Kernel-based interpolants are represented using a number of parameters that is linear in the size of the input, whereas overparameterized neural networks require many more parameters than points. *(iv)* The inductive bias of kernel methods can be characterized explicitly via the RKHS norm. We provide explicit expressions for these kernels and their RKHS norms and we argue that they can be viewed as multidimensional generalization of cubic spline interpolation in 1D. We further demonstrate that Poisson Surface reconstruction can itself be viewed as a kernel method and give an expression for its RKHS norm.

1.1 Related Work

Methods for 3D surface reconstruction can mostly be divided by their choice of surface representation: These are *(i)* the zero level set of a volumetric scalar function [20, 3, 13, 23, 25, 7], *(ii)* the fixed point of a projection operator onto locally fitted patches [1, 14, 18], *(iii)* a mesh connecting the input points [17], or *(iv)* a collection of local parametric maps e.g. [29, 15, 11, 12]. For a recent up-to-date survey of surface reconstruction techniques, we refer the reader to [5].

The “random feature” kernels that we use in this paper, which arise from training the top-layer weights in two-layer networks of infinite width, were described in [10, 22]. More recently, a lot of work has focused on a different kernel, known as the “neural tangent kernel” [19, 9], that linearly approximates the training of *both* layers of a neural network. We chose to use random feature kernels since, when the input dimension is small, typical initializations in neural networks lead to mainly training the top layer weights. More broadly, the function spaces associated with shallow neural networks were studied in [4, 6, 24, 27, 30].

2 Neural Spline Formulation

We formulate the problem of surface reconstruction as the task of finding a scalar function $f : \mathbb{R}^3 \rightarrow \mathbb{R}$ whose zero level set $S = \{p : f(p) = 0\} \subset \mathbb{R}^3$ is the estimated surface (see Figure 1). In its most general form in arbitrary dimensions, we write our problem as follows.

We assume we are given a set of s input points $\mathcal{X} = \{x_j\}_{j=1}^s \subset \mathbb{R}^d$, function values $\mathcal{Y} = \{y_j\}_{j=1}^s \subset \mathbb{R}$, and vectors $\mathcal{N} = \{n_j\}_{j=1}^s \subset \mathbb{R}^d$. Our goal is to optimize an objective function of the form:

$$\min_{\theta \in \mathbb{R}^{d_\theta}} L(\theta), \quad \text{with} \quad L(\theta) = \frac{1}{2} \sum_{j=1}^s |f(x_j; \theta) - y_j|^2 + \|\nabla_x f(x_j; \theta) - n_j\|^2. \quad (1)$$

Here $f(x; \theta)$ is a family of functions $\mathbb{R}^d \rightarrow \mathbb{R}$ parameterized by $\theta \in \mathbb{R}^{d_\theta}$. For surface reconstruction, we have $d = 3$ and $y_j = 0$, since the reconstructed surface is given by the zero level set.

We begin by introducing the Neural Spline family of functions through the lens of finite-width shallow neural networks in Section 2.1, and turn to the infinite-width limit formulation in Section 2.2. While

our approach is simple and our derivations straightforward, we differ slightly from a standard kernel regression setting since we employ a multi-dimensional kernel that includes the gradient of the fitted function. This formulation allows us to fit points and normals simultaneously.

2.1 Finite-Width Kernel

We first assume that the model $f(x; \theta)$ is a two-layer ReLU neural network with m neurons, but we keep the bottom layer weights *fixed* from initialization:

$$f(x; \theta) = \frac{1}{\sqrt{m}} \sum_{i=1}^m c_i [a_i^T x + b_i]_+, \quad \theta = (c_1, \dots, c_m) \in \mathbb{R}^m. \quad (2)$$

Here we write $[z]_+ = \max(z, 0)$ for the ReLU function. The weights $(a_{i1}, \dots, a_{id}, b_i) \in \mathbb{R}^{d+1}$ are *fixed* randomly according to some specified distribution.

Remark 1. In typical initialization schemes for neural networks (e.g., Kaiming He initialization [16]), the weights of each layer are initialized with a variance that is inversely proportional to the number of inputs of that layer. Our choice of fixing (a_i, b_i) is motivated by the fact that using a standard two-layer network, for a given target model and as $m \rightarrow \infty$, only the top layer weights tend to vary throughout training [30]. Figure 5 shows how a deep MLP produces very similar results to our kernel reconstruction.

Our model (2) is linear in the parameters θ , so our objective function $L(\theta)$ is *convex*. However, since we assume $m \gg s$, we expect to have an infinite set of global minimizers (an affine subspace in \mathbb{R}^{d_θ}). Our goal is to find the minimizer with smallest parameter norm:

$$\theta^* = \arg \min \{ \|\theta\|^2 : \theta \in \mathbb{R}^{d_\theta} \ L(\theta) = 0 \}.$$

This minimizer is given explicitly by $\theta^* = W^\dagger \delta$ where W^\dagger denotes the Moore-Penrose pseudo-inverse of W and

$$W = \frac{1}{\sqrt{m}} \begin{bmatrix} [a_j^T x_i + b_j]_+ \\ \mathbf{1}[a_j^T x_i + b_j]a_j \end{bmatrix}_{\substack{i=1, \dots, s \\ j=1, \dots, m}} \in \mathbb{R}^{(s+ds) \times m}, \quad \delta = \begin{bmatrix} y_i \\ n_i \end{bmatrix}_{i=1, \dots, s} \in \mathbb{R}^{s+ds}.$$

If W has full rank, then $W^\dagger = W^T (WW^T)^{-1}$ and we can equivalently look for $z^* \in \mathbb{R}^{(s+ds)}$ such that $K_{\mathcal{X}} z^* = W\theta^* = \delta$ where $K_{\mathcal{X}} = WW^T \in \mathbb{R}^{(s+ds) \times (s+ds)}$. Note that $K_{\mathcal{X}}$ can be viewed as a Gram matrix associated with the multi-dimensional kernel

$$K(x, x') = \frac{1}{m} \sum_{i=1}^m \begin{bmatrix} [a_i^T x + b_i]_+ [a_i^T x' + b_i]_+ & [a_i^T x + b_i]_+ \mathbf{1}[a_i^T x' + b_i]a_i^T \\ \mathbf{1}[a_i^T x + b_i] [a_i^T x' + b_i]_+ a_i & \mathbf{1}[a_i^T x + b_i] \mathbf{1}[a_i^T x' + b_i] a_i a_i^T \end{bmatrix} \in \mathbb{R}^{(d+1) \times (d+1)}. \quad (3)$$

2.2 Infinite-Width Kernel

As the number of neurons m tends to infinity, the kernel (3) converges to

$$K_\infty(x, x') = \mathbb{E}_{(a,b)} \begin{bmatrix} [a^T x + b]_+ [a^T x' + b]_+ & [a^T x + b]_+ \mathbf{1}[a^T x' + b]a^T \\ \mathbf{1}[a^T x + b] [a^T x' + b]_+ a & \mathbf{1}[a^T x + b] \mathbf{1}[a^T x' + b] a a^T \end{bmatrix} \in \mathbb{R}^{(d+1) \times (d+1)}. \quad (4)$$

We use this kernel to characterize the interpolant in the infinite-width limit. For this, we simply replace K in (3) with K_∞ and solve the linear system the described in the previous section. More concretely (and rearranging terms), our goal is to recover $\alpha_1^*, \dots, \alpha_s^* \in \mathbb{R}^{d+1}$ such that

$$\sum_{i=1}^s K_\infty(x_j, x_i) \alpha_i^* = \begin{bmatrix} y_j \\ n_j \end{bmatrix} \in \mathbb{R}^{d+1}, \quad j = 1, \dots, s. \quad (5)$$

Our final interpolant f^* is such that $\begin{bmatrix} f^*(x) \\ \nabla f^*(x) \end{bmatrix} = K_\infty(x, x_i) \alpha_i^*$ for all $x \in \mathbb{R}^d$. The function f^* can also be viewed as the solution to

$$\begin{aligned} & \underset{f \in \mathcal{H}}{\text{minimize}} \quad \|f\|_{\mathcal{H}}, \\ & \text{subject to} \quad f(x_i) = 0 \text{ and } \nabla f(x_i) = n_i \end{aligned} \quad (6)$$

where \mathcal{H} is the RKHS corresponding to the one-dimensional kernel $\mathbb{E}_{(a,b)}[a^T x + b]_+[a^T x' + b]_+$. In Section 3.3 we give an expression for the norm $\|\cdot\|_{\mathcal{H}}$ that defines the inductive bias of solutions. In Appendix A, we provide analytic expressions for the kernel (4) for two natural distributions for (a, b) :

$$\text{Uniform initialization:} \quad a \sim \mathcal{U}[\mathbb{S}^{d-1}], \quad b \sim \mathcal{U}[-k, k], \quad (7)$$

$$\text{Gaussian initialization:} \quad (a, b) \sim \mathcal{N}(0, Id_d). \quad (8)$$

The uniform distribution (7) corresponds to the default initialization of linear layers in Pytorch and, as we argue in Section 3.1, it leads to a direct generalization of cubic spline interpolation. However, the Gaussian initialization actually leads to simpler analytical expressions for K_{∞} and produces almost the same results. We refer to Appendix A for a discussion and comparison.

3 Discussion

3.1 Connection to Cubic Splines in 1D

When $d = 1$, the uniform initialization (7) is such that $a \sim \mathcal{U}(\mathbb{S}^0) = \mathcal{U}(\{-1, 1\})$, and the first element in K_{∞} is simply

$$\begin{aligned} K_{\text{spline}}(x, x') &= \frac{1}{2} \int_{-k}^k [x + b]_+[x' + b]_+ db + \frac{1}{2} \int_{-k}^k [-x + b]_+[-x' + b]_+ db \\ &= \frac{1}{12} (3x' - x + 2k)(x + k)^2 + \frac{1}{12} (-3x + x' + 2k)(x' - k)^2 \quad \text{if } -k \leq x \leq x' \leq k, \end{aligned} \quad (9)$$

where the expression for $-k \leq x' < x \leq k$ is obtained by swapping x and x' . For fixed x , the map $K_{\text{spline}}(x, \cdot)$ is piecewise cubic and twice continuously differentiable (C^2). This implies that kernel regression with (9) yields *cubic spline interpolation*. Applying the Neural Spline objective (1) with derivative constraints at the samples in $d = 1$ also yields a piecewise cubic interpolant, although this curve is in general only C^1 . For other distributions of a and b , the kernel is no longer cubic, but the norm in the RKHS is a weighed norm of curvature (see [30] for details). In this sense, our approach with the initialization (7) can be viewed as a multi-dimensional version of spline interpolation.

3.2 Regularization and Robustness to Noise

To deal with noisy data, we can optionally add a simple regularizer term to our formulation that corresponds to penalizing the RKHS norm of the interpolant (“kernel ridge regression”). Concretely, we replace (5) with

$$\sum_{i=1}^s K_{\infty}(x_j, x_i) \alpha_i^* + \delta_{ij} \lambda Id_{d+1} = \begin{bmatrix} y_j \\ n_j \end{bmatrix} \in \mathbb{R}^{d+1}, \quad j = 1, \dots, s. \quad (10)$$

The regularizer term affects the spectrum of the Gram matrix $K_{\infty}(x_j, x_i)$ by smoothing its smallest eigenvalues, with a similar effect to early stopping in gradient descent (see e.g. [2]). Figures 2 and 3 show an example of applying this regularizer on 2D and 3D problems.

3.3 Inductive Bias of Interpolants

Our interpolant function f^* belongs to the Hilbert space given by

$$\begin{aligned} \mathcal{H} &= \left\{ f(x) = \int c(a, b)[ax + b]_+ d\tau(a, b) : \|f\|_{\mathcal{H}} < +\infty \right\}. \\ \text{where } \|f\|_{\mathcal{H}}^2 &= \inf \left\{ \int c(a, b)^2 d\tau(a, b) : f(x) = \int c(a, b)[ax + b]_+ d\tau(a, b) \right\}, \end{aligned} \quad (11)$$

where $\tau(a, b)$ is a measure over the weights a and b (e.g., (7) or (8)). The inductive bias of our interpolation method is thus determined by the RKHS norm in (11) since our method outputs the interpolating function which minimizes that norm. As noted in [24], if $f(x) = \int c(a, b)[ax + b]_+ d\tau(a, b)$ and $d\tau(a, b) = d\tau_a(a)d\tau_b(b)$, then by differentiating twice we have that

$$\Delta f(x) = \int c(a, b) \delta(ax + b) d\tau(a, b) = \int_{\{ax+b=0\}} c(a, b) d\tau_a(a). \quad (12)$$

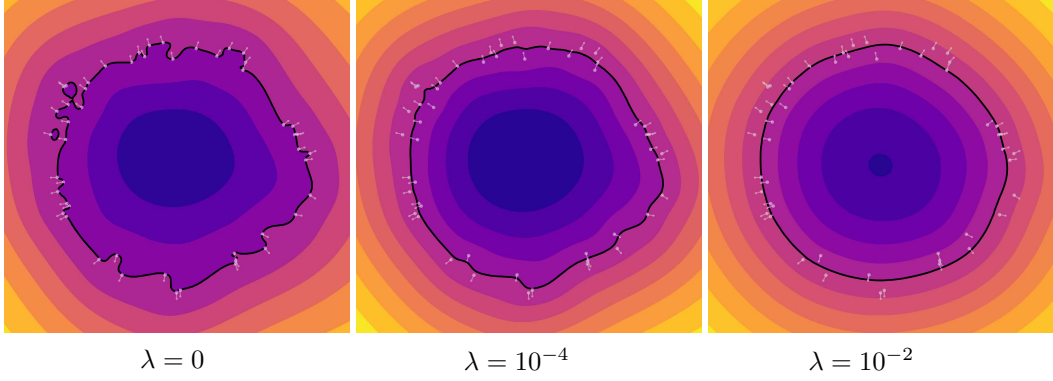


Figure 2: *The effect of adding a regularization in 2D.* In the left image, fitting the points and normals with no regularization and yields a curve which interpolates the noisy input data. Larger values of λ (the middle and right images) lead to smoother solutions which do not interpolate noise in the input.

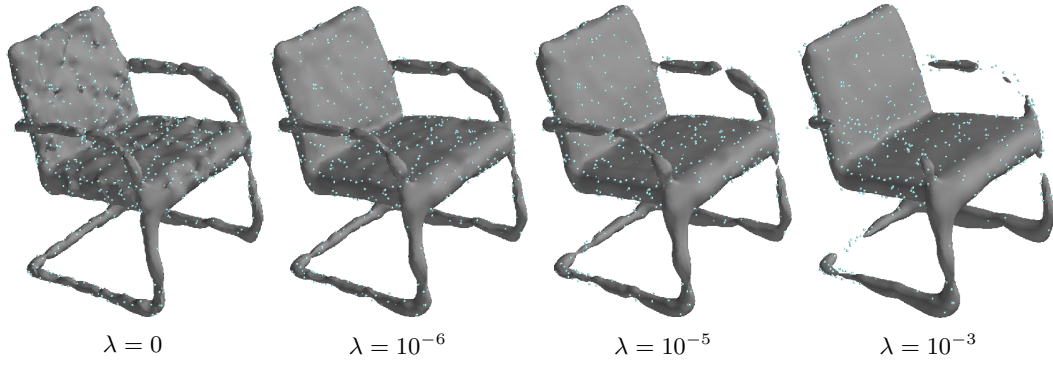


Figure 3: *The effect of adding a regularization in 3D.* In the left image, fitting the points and normals with no regularization and yields a surface which interpolates the noisy input data. Larger values of λ (the three right images) lead to smoother solutions which do not interpolate noise in the input. If λ is too large, the output loses geometric details (e.g., the arms and base of the chair in the right image).

By comparing (11) and (12), we see that the RKHS norm and the Laplacian of f are closely related. More precisely, the right hand side of (12) is essentially the (dual) *Radon Transform* of Δf . Under certain assumptions, the Radon Transform can also be inverted. We report the following statement from [24].

Proposition 2 (Ongie et al. [24]). *Let $f(x) = \int c(a, b)[ax + b]_+ d\tau(a, b)$. If we assume that $c(a, b) = c(-a, -b)$ holds, then*

$$c(a, b) = \gamma_d \frac{\mathcal{R}\{(-\Delta)^{\frac{d+1}{2}} f(x)\}(a, b)}{\tau(a, b)},$$

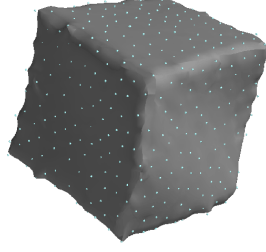
where $\mathcal{R}\{f\}(a, b)$ is the Radon Transform of f and $\gamma_d = \frac{1}{2(2\pi)^{d-1}}$.

3.4 Poisson Surface Reconstruction as a Kernel

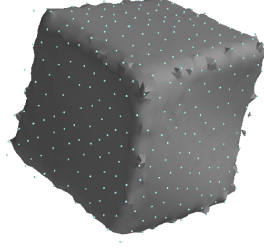
We cast Screened Poisson Surface Reconstruction [20] in the kernel form to facilitate comparisons. In its simplest form, Poisson reconstruction of a surface, extracts the level set of a smoothed indicator function determined as the solution of

$$-\Delta f = \nabla \cdot V$$

where V is a vector field obtained from normals n_i at samples x_i , and we use f to denote the (smoothed) indicator function as it plays the same role as f in (1). The equation above is closely related to (1): specifically, it is the equation for the minimizer of $\int_{\mathbb{R}^3} \|\nabla_x f(x) - V\|^2 dx$ and the second term in (1) can be viewed as an approximation of this term by sampling at x_i . The screened form of Poisson reconstruction effectively adds the first term with $y_i = 0$, as the indicator function



Approximate Poisson Kernel



Poisson Surface Reconstruction

Figure 4: *Left*: Poisson reconstruction using the approximate Kernel (14). *Right*: Screened Poisson Reconstruction of the same input.

at points of interest is supposed to be zero. For the Poisson equation, the solution can be explicitly written as an integral

$$f(x) = \int_{\mathbb{R}^3} \frac{\nabla_z \cdot V(z) dz}{|x - z|}.$$

The vector field V is obtained by interpolating the normals using a fixed-grid spline basis and barycentric coordinates of the sample points with respect to the grid cell containing it. This is equivalent to using a non-translation invariant non-symmetric locally-supported kernel $K_B(z, x)$:

$$V(z) = \sum_i K_B(z, x_i) n_i.$$

Lemma 3. *Let $\{c_j \in \mathbb{R}^3\}_{j=1}^g$ be a set of points arranged on a regular grid, $B_1(x - z)$ be the trilinear basis function, and $B_n(x - z)$ be a degree- n spline basis function (See Appendix C for equations for B_1 and B_n). The kernel corresponding to Poisson Surface Reconstruction is*

$$K_{\text{PR}}(x, x') = \int_{\mathbb{R}^3} \frac{K_B(z, x') dz}{|x - z|}, \quad K_B(z, x) = \sum_j B_1(x - c_j) B_n(z - c_j). \quad (13)$$

To study the qualitative properties of this kernel, we replace $K_B(z, x)$ with a radial kernel $B_n^1(|z - x|)$ (see Appendix C) which has qualitatively similar behavior (see Figure 4). Since both B_n^1 and the Laplace kernel $\frac{1}{|x - z|}$ are radial functions, their convolution is also radial, yielding a translation-invariant radial approximation $K_{\text{PR}}^{\text{approx}}$ of K_{PR} :

$$K^{\text{approx}}(x, x') = \int_{\mathbb{R}^3} \frac{B_n^1(|z - x'|) dz}{|x - z|}. \quad (14)$$

Lemma 4. *The RKHS norm of the corresponding to the approximate Poisson kernel $K_{\text{PR}}^{\text{approx}}$ is*

$$\|f\|_{\mathcal{H}} = \int \frac{|\mathcal{F}[f]|^2}{\mathcal{F}[K^{\text{approx}}]} d\omega \quad (15)$$

where $\mathcal{F}[\cdot]$ is the Fourier transform.

We discuss the kernel formulation of Poisson Reconstruction in more detail in Appendix C.

4 Experiments and Results

We now demonstrate the effectiveness of Neural Splines on the task of surface reconstruction. For all the experiments in this section, we used the analytical form of the kernel (4) with uniform initialization (7) unless stated otherwise. We compared the uniform (7) and Gaussian (8) initializations quantitatively and qualitatively in Appendix D.3, showing almost no measurable difference between the reconstructions produced by either initialization. We compare the empirical and analytical kernels in detail in Appendix D.2. Code for all the experiments in this section is available at <https://url.redacted.for.submission>.

Data Centering and Scaling. We note that both the Gaussian and Uniform Kernels are rotation invariant (i.e. $K(Rx, Rx') = K(x, x')$ for some rotation matrix R), but are *not* translation invariant. To address this issue, we center and scale all the input points to have mean zero and lie in $[-\frac{1}{2}, \frac{1}{2}]^3$. We undo these transformations when returning the results.

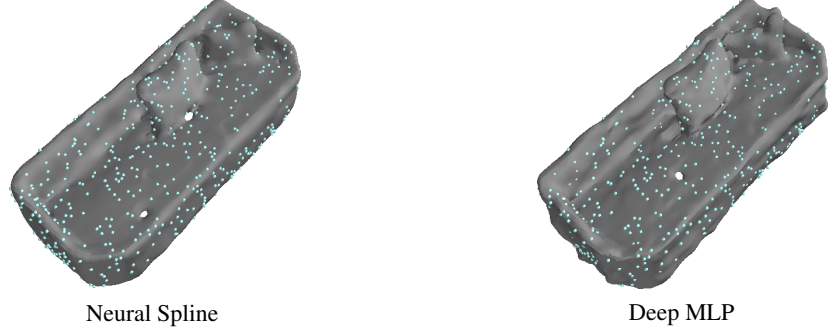


Figure 5: *Left*: The surface fitted to the blue points using a Neural Spline. *Right*: The surface fitted using a deep MLP with ReLU activations. The MLP was trained with full-batch gradient descent on the input data for 100k iterations using the objective (1).

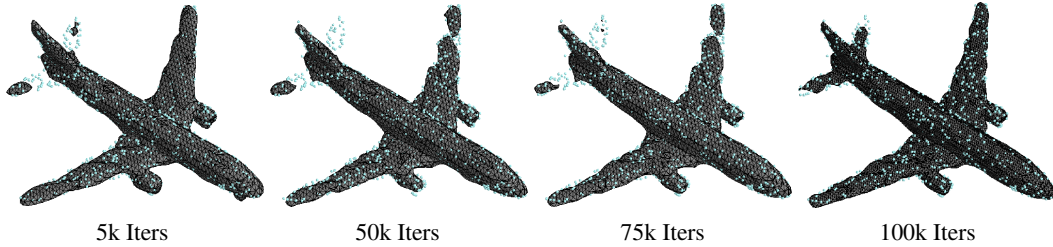


Figure 6: Eikonal Reconstruction shows only marginal improvements (*e.g.*, the tail of the airplane) between 5k and 100k iterations, due to the slow convergence of gradient descent.

Neural Networks versus Neural Splines. We demonstrate that Neural Splines are just as effective as using a full neural network. Figure 5 shows an example of a shape fit with a 4 layer MLP (3 - 512 - 512 - 1) and the same shape fit with a Neural Spline. We initialized the MLP with the geometric initialization proposed in [3] and trained it on the objective (1) for 100k iterations using Adam [21] with a learning rate of 0.001, taking a total time of 1 hour on an NVIDIA-1080-Ti GPU. In contrast, the Neural Spline surface took under 1 minute to fit and extract the surface on the same hardware.

4.1 Quantitative Benchmark

To evaluate the effectiveness of Neural Splines for surface reconstruction, we performed a quantitative evaluation on a subset of the ShapeNet dataset [8]. We used 1024 random points and normals sampled from the surface of 20 shapes per category across 13 categories (totalling 260 shapes). We evaluated our method against Screened Poisson Surface Reconstruction (SPSR) and the Eikonal Reconstruction method in [13], which is a state-of-the-art neural network based method.

As criteria for the benchmark, we consider the Intersection over Union (IoU) and Chamfer Distance between the reconstructed shapes and the ground truth shapes. The former metric captures the accuracy of the predicted occupancy function, while the latter metric captures the accuracy of the predicted surface. We report the results of this experiment in Table 1. We report per-category results in Appendix D.1. Figure 7 shows visual results from the benchmark for a few models. Appendix D.4 shows figures of reconstructions from each ShapeNet class in the benchmark.

Screened Poisson Surface Reconstruction. SPSR has a number of parameters that can be adjusted to affect the quality of the reconstruction. For our benchmark, we performed a grid search over a range of these parameters, choosing for each shape the ones which maximized each metric under consideration. Specifically, we considered the *octree depth* in [6, 7, 8, 9], the number of *points per leaf* in [1, 2, 3, 5, 10], the *point weight*, which controls the degree to which the method interpolates the input, in [4.0, 100.0, 1000.0]. Since all the shapes in the benchmark are watertight meshes, we used Dirichlet boundary constraints for the reconstruction.

Eikonal Reconstruction. For Eikonal Reconstruction, we trained each model for 5000 iterations with Adam and a learning rate of 0.001 using the same parameters proposed in the original paper [13]. We included the normals in the loss with the parameter τ set to 1. The Eikonal regularization term λ was set to 0.1. While Eikonal reconstruction can benefit slightly from using a larger number of

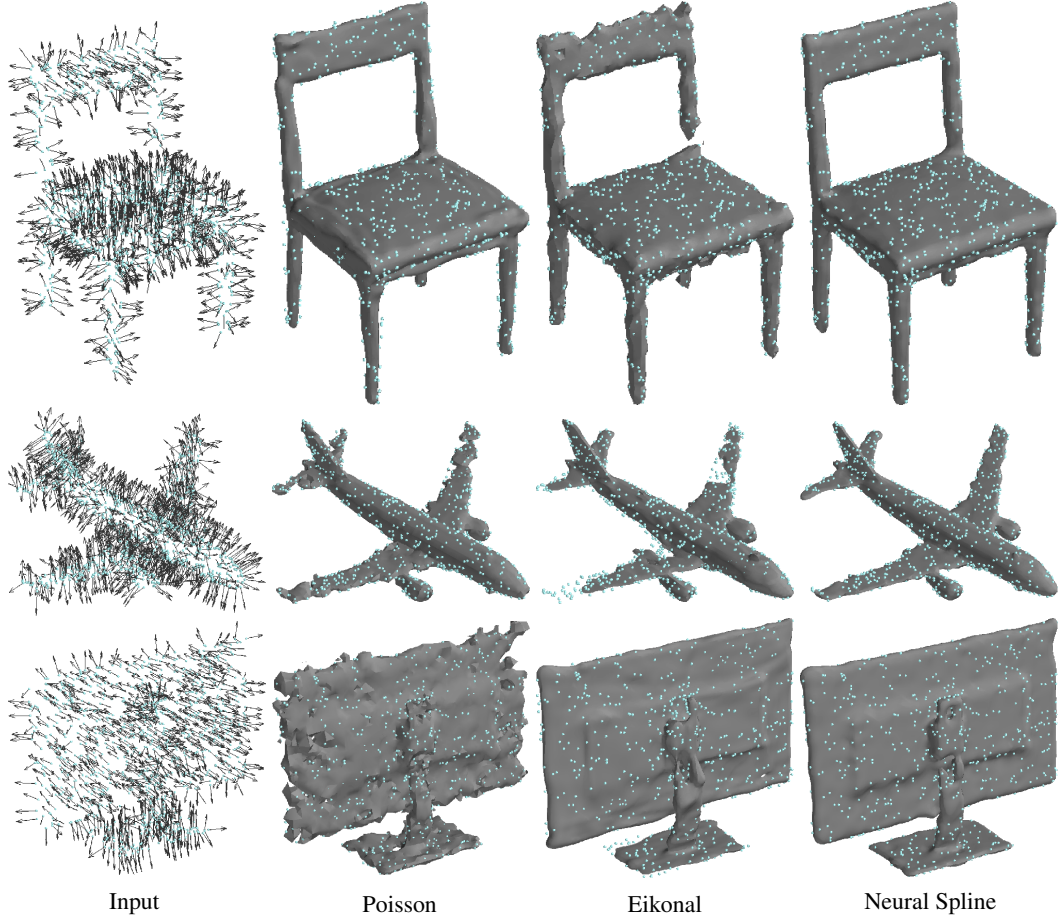


Figure 7: *Comparisons between reconstruction techniques on ShapeNet models. Left Column:* The input points and normals, *Right Columns:* The surfaces reconstructed by each method. The figures for Poisson are the models with lowest Chamfer distance in the parameter sweep. Figures from all the ShapeNet classes are shown in Appendix D.4

Metric	Poisson			Eikonal			Neural Spline		
	mean	median	std	mean	median	std	mean	median	std
Chamfer	2.22e-4	1.70e-4	1.76e-4	6.66e-4	1.07e-4	4.69e-3	5.32e-5	4.07e-5	3.53e-5
IoU	0.6340	0.6728	0.1577	0.8213	0.8566	0.1461	0.9167	0.9438	0.0985

Table 1: Quantitative comparison of the Chamfer Distance and Intersection over Union between Neural Splines, Screened Poisson Surface Reconstruction [20], and Eikonal Reconstruction [13] over a subset of the ShapeNet dataset.

iterations, doing so is prohibitively slow over many models. Figure 6 shows only slight improvements between 5k and 100k iterations, which required 2 hours of fitting on a NVIDIA-1080-Ti GPU.

5 Conclusion and Future Work

In this work, we have shown that Neural Spline kernels arising from infinitely wide shallow ReLU networks can be very effective tools for 3D surface reconstruction, outperforming state of the art methods while being computationally efficient and conceptually simple. In some sense, our work bridges the gap between traditional reconstruction methods and modern neural network based methods since it leverages the deep connection between neural networks and kernels methods.

In the future, we hope to integrate Neural Splines into deep learning pipelines and apply them to other 3D tasks such as shape completion and sparse reconstruction. On the theory side, we would like to investigate and compare the approximation properties of different kernels in the context of 3D reconstruction, by building on existing work on kernel function spaces such as [4].

Broader Impact

Our work uses kernels that are inspired by neural networks for the task 3D surface reconstruction. While other methods for solving this task exist, our approach improves the current state of the art and could lead to a more effective and widespread use of 3D reconstruction methods in real-life applications. Surface reconstruction is in fact a core technology in a variety of practical domains, including computer aided geometric design (CAGD), robotics, autonomous driving, reverse engineering, architectural analysis, medical imaging, and augmented reality.

While robust, high quality surface reconstruction opens the door to many exciting applications, like any technology, it can be used for nefarious purposes. In particular, as with many advances in imaging, our 3D surface reconstruction method could be used by corporations and governments in surveillance systems deployed without their targets' consent.

Acknowledgements

This work is partially supported by the Alfred P. Sloan Foundation, NSF RI-1816753, NSF CAREER CIF 1845360, NSF CHS-1901091, Samsung Electronics, and the Institute for Advanced Study.

References

- [1] Anders Adamson and Marc Alexa. Approximating and intersecting surfaces from points. In *Proceedings of the 2003 Eurographics/ACM SIGGRAPH symposium on Geometry processing*, pages 230–239. Eurographics Association, 2003.
- [2] Alnur Ali, J. Zico Kolter, and Ryan J. Tibshirani. A Continuous-Time View of Early Stopping for Least Squares. *arXiv:1810.10082 [cs, stat]*, February 2019.
- [3] Matan Atzmon and Yaron Lipman. Sal: Sign agnostic learning of shapes from raw data, 2019.
- [4] Francis Bach. Breaking the curse of dimensionality with convex neural networks. *Journal of Machine Learning Research*, 18(19):1–53, 2017.
- [5] Matthew Berger, Andrea Tagliasacchi, Lee M Seversky, Pierre Alliez, Gael Guennebaud, Joshua A Levine, Andrei Sharf, and Claudio T Silva. A survey of surface reconstruction from point clouds. In *Computer Graphics Forum*, volume 36, pages 301–329. Wiley Online Library, 2017.
- [6] Alberto Bietti and Julien Mairal. On the Inductive Bias of Neural Tangent Kernels. *arXiv:1905.12173 [cs, stat]*, October 2019.
- [7] Rohan Chabra, Jan Eric Lenssen, Eddy Ilg, Tanner Schmidt, Julian Straub, Steven Lovegrove, and Richard Newcombe. Deep local shapes: Learning local sdf priors for detailed 3d reconstruction, 2020.
- [8] Angel X. Chang, Thomas Funkhouser, Leonidas Guibas, Pat Hanrahan, Qixing Huang, Zimo Li, Silvio Savarese, Manolis Savva, Shuran Song, Hao Su, Jianxiong Xiao, Li Yi, and Fisher Yu. Shapenet: An information-rich 3d model repository, 2015.
- [9] Lenaic Chizat, Edouard Oyallon, and Francis Bach. On lazy training in differentiable programming. In *Advances in Neural Information Processing Systems*, pages 2933–2943, 2019.
- [10] Youngmin Cho and Lawrence K Saul. Kernel methods for deep learning. In *Advances in neural information processing systems*, pages 342–350, 2009.
- [11] Theo Deprelle, Thibault Groueix, Matthew Fisher, Vladimir G. Kim, Bryan C. Russell, and Mathieu Aubry. Learning elementary structures for 3d shape generation and matching, 2019.
- [12] Matheus Gadelha, Rui Wang, and Subhransu Maji. Deep manifold prior, 2020.
- [13] Amos Gropp, Lior Yariv, Niv Haim, Matan Atzmon, and Yaron Lipman. Implicit geometric regularization for learning shapes, 2020.
- [14] Gaël Guennebaud and Markus Gross. Algebraic point set surfaces. In *ACM SIGGRAPH 2007 papers*, pages 23–es. ACM New York, NY, USA, 2007.
- [15] Rana Hanocka, Gal Metzer, Raja Giryes, and Daniel Cohen-Or. Point2mesh: A self-prior for deformable meshes, 2020.

- [16] Kaiming He, Xiangyu Zhang, Shaoqing Ren, and Jian Sun. Delving deep into rectifiers: Surpassing human-level performance on imagenet classification. *2015 IEEE International Conference on Computer Vision (ICCV)*, Dec 2015. doi: 10.1109/iccv.2015.123. URL <http://dx.doi.org/10.1109/ICCV.2015.123>.
- [17] Hugues Hoppe, Tony DeRose, Tom Duchamp, John McDonald, and Werner Stuetzle. Surface reconstruction from unorganized points. In *Proceedings of the 19th annual conference on Computer graphics and interactive techniques*, pages 71–78, 1992.
- [18] Hui Huang, Shihao Wu, Minglun Gong, Daniel Cohen-Or, Uri Ascher, and Hao Zhang. Edge-aware point set resampling. *ACM transactions on graphics (TOG)*, 32(1):1–12, 2013.
- [19] Arthur Jacot, Franck Gabriel, and Clément Hongler. Neural tangent kernel: Convergence and generalization in neural networks, 2018.
- [20] Michael Kazhdan and Hugues Hoppe. Screened poisson surface reconstruction. *ACM Transactions on Graphics (ToG)*, 32(3):1–13, 2013.
- [21] Diederik P. Kingma and Jimmy Ba. Adam: A method for stochastic optimization, 2014.
- [22] Nicolas Le Roux and Yoshua Bengio. Continuous neural networks. In *Artificial Intelligence and Statistics*, pages 404–411, 2007.
- [23] Lars Mescheder, Michael Oechsle, Michael Niemeyer, Sebastian Nowozin, and Andreas Geiger. Occupancy networks: Learning 3d reconstruction in function space. *2019 IEEE/CVF Conference on Computer Vision and Pattern Recognition (CVPR)*, Jun 2019. doi: 10.1109/cvpr.2019.00459. URL <http://dx.doi.org/10.1109/CVPR.2019.00459>.
- [24] Greg Ongie, Rebecca Willett, Daniel Soudry, and Nathan Srebro. A function space view of bounded norm infinite width relu nets: The multivariate case, 2019.
- [25] Jeong Joon Park, Peter Florence, Julian Straub, Richard Newcombe, and Steven Lovegrove. DeepSDF: Learning continuous signed distance functions for shape representation. *2019 IEEE/CVF Conference on Computer Vision and Pattern Recognition (CVPR)*, Jun 2019. doi: 10.1109/cvpr.2019.00025. URL <http://dx.doi.org/10.1109/CVPR.2019.00025>.
- [26] Alexander D Poularikas. *Transforms and applications handbook*. CRC press, 2018.
- [27] Pedro Savarese, Itay Evron, Daniel Soudry, and Nathan Srebro. How do infinite width bounded norm networks look in function space?, 2019.
- [28] Donald C Solmon. Asymptotic formulas for the dual radon transform and applications. *Mathematische Zeitschrift*, 195(3):321–343, 1987.
- [29] Francis Williams, Teseo Schneider, Claudio Silva, Denis Zorin, Joan Bruna, and Daniele Panozzo. Deep geometric prior for surface reconstruction. *2019 IEEE/CVF Conference on Computer Vision and Pattern Recognition (CVPR)*, Jun 2019. doi: 10.1109/cvpr.2019.01037. URL <http://dx.doi.org/10.1109/CVPR.2019.01037>.
- [30] Francis Williams, Matthew Trager, Claudio Silva, Daniele Panozzo, Denis Zorin, and Joan Bruna. Gradient dynamics of shallow univariate relu networks, 2019.

A Derivation of the Infinite Width Kernel

A.1 Uniform Initialization

We derive an explicit expression for the kernel K_∞ in (4) in the case of uniform initialization (7). We first prove the following Lemma which we will use in our calculations.

Lemma 5. *Assume that $\mathcal{F} : \mathbb{R} \times \mathbb{R} \rightarrow \mathbb{R}$ is such that $\mathcal{F}(ks, kt) = k^r \mathcal{F}(s, t)$ for some r and any $k \geq 0$. For any $x, x' \in \mathbb{R}^d$ we have that*

$$\begin{aligned} \int_{a \in \mathbb{S}^{d-1}} \mathcal{F}(a^T x, a^T x') d\Omega &= \eta_{d,r} \cdot \frac{r!!}{(d+r-2)!!} \cdot F_1 \\ \int_{a \in \mathbb{S}^{d-1}} a \mathcal{F}(a^T x, a^T x') d\Omega &= \eta_{d,r} \cdot \frac{(r+1)!!}{(d+r-1)!!} \cdot Q^T \begin{bmatrix} 0_{d-2} \\ F_{\cos} \\ F_{\sin} \end{bmatrix} \\ \int_{a \in \mathbb{S}^{d-1}} aa^T \mathcal{F}(a^T x, a^T x') d\Omega &= \eta_{d,r} \cdot \frac{(r+2)!!}{(d+r)!!} \cdot Q^T \begin{bmatrix} \frac{1}{r+2} Id_{d-2} & 0 & 0 \\ 0 & F_{\cos^2} & F_{\sin \cos} \\ 0 & F_{\sin \cos} & F_{\sin^2} \end{bmatrix} Q \end{aligned} \quad (16)$$

where $F_g = \int_0^{2\pi} g(\psi) \mathcal{F}(\|x\| \cos(\psi), \|x'\| \cos(\psi - \alpha)) d\psi$ (for $g = 1, \cos, \cos^2$, etc.), $Q \in SO(d)$ is such that $Qx = (0, \dots, \|x\|, 0)^T, Qx' = (0, \dots, \|x'\| \cos(\alpha), \|x'\| \sin(\alpha))^T$ and

$$\eta_{d,r} = \begin{cases} 2^{\lceil \frac{d-2}{2} \rceil} \pi^{\lfloor \frac{d-2}{2} \rfloor} & \text{if } r \text{ is even,} \\ 2^{\lfloor \frac{d-2}{2} \rfloor} \pi^{\lceil \frac{d-2}{2} \rceil} & \text{if } r \text{ is odd.} \end{cases}$$

Proof. If $Q \in SO(d)$ then by change of variables $a = Q^T \tilde{a}$ we have that

$$\begin{aligned} \int_{a \in \mathbb{S}^{d-1}} aa^T \mathcal{F}(a^T x, a^T x') d\Omega &= \int_{\tilde{a} \in \mathbb{S}^{d-1}} Q^T \tilde{a} \tilde{a}^T Q \mathcal{F}(\tilde{a}^T Qx, \tilde{a}^T Qx') d\Omega \\ &= Q^T \left(\int_{\tilde{a} \in \mathbb{S}^{d-1}} \tilde{a} \tilde{a}^T \mathcal{F}(\tilde{a}^T \tilde{x}, \tilde{a}^T \tilde{x}') d\Omega \right) Q, \end{aligned}$$

where $\tilde{x} = Qx$. Without loss of generality we thus assume that $x = (0, \dots, \|x\|, 0)^T$ and $x' = (0, \dots, \|x'\| \cos(\alpha), \|x'\| \sin(\alpha))^T$ where $\alpha = \arccos(x^T x' / \|x\| \|x'\|) \in [0, \pi]$. We now adopt hyperspherical coordinates $(\theta_1, \dots, \theta_{d-2}, \psi)$ where $\theta_i \in [0, \pi]$ and $\psi \in [0, 2\pi]$. The conversion between cartesian and spherical coordinates is given by:

$$\begin{aligned} a_1 &= \cos(\theta_1) \\ a_2 &= \sin(\theta_1) \cos(\theta_2) \\ &\vdots \\ a_{d-1} &= \sin(\theta_1) \dots \sin(\theta_{d-2}) \cos(\psi) \\ a_d &= \sin(\theta_1) \dots \sin(\theta_{d-2}) \sin(\psi) \end{aligned}$$

We also have that

$$\begin{aligned} d\Omega &= \sin^{d-2}(\theta_1) \sin^{d-3}(\theta_2) \dots \sin(\theta_{d-2}) d\theta_1 d\theta_2 \dots d\psi \\ a \cdot x &= a_{d-2} \\ &= \|x\| \sin(\theta_1) \dots \sin(\theta_{d-2}) \cos(\psi) \\ a \cdot x' &= a_{d-2} \\ &= a_{d-2} \|x'\| \cos(\alpha) + a_{d-1} \|x'\| \sin(\alpha) \\ &= \|x'\| \sin(\theta_1) \dots \sin(\theta_{d-2}) (\cos(\psi) \cos(\alpha) + \sin(\psi) \sin(\alpha)) \\ &= \|x'\| \sin(\theta_1) \dots \sin(\theta_{d-2}) \cos(\psi - \alpha) \end{aligned}$$

We now consider the integral $\int aa^T \mathcal{F}(a^T x, a^T x') d\Omega$. For any two indices $i \leq j \leq d-2$, we have

$$\begin{aligned}
& \int_{a \in \mathbb{S}^{d-1}} a_i a_j \mathcal{F}(a \cdot x, a \cdot x') d\Omega \\
&= \int_0^{2\pi} \dots \int_0^\pi \sin^{d-2+r}(\theta_1) \dots \sin^{1+r}(\theta_{d-2}) a_i a_j \mathcal{F}(\|x\| \cos \psi, \|x'\| \cos(\psi - \alpha)) d\psi d\theta_1, \dots, d\theta_{d-2} \\
&= \int_0^\pi \sin^{d-2+r+2}(\theta_1) d\theta_1 \dots \int_0^\pi \sin^{(d-1-i)+r+1}(\theta_i) \cos(\theta_i) d\theta_i \dots \int_0^\pi \sin^{(d-1-j)+r}(\theta_j) \cos(\theta_j) d\theta_j \\
&\quad \dots \int_0^\pi \sin^{(d-1-(j+1))+r}(\theta_{j+1}) d\theta_{j+1} \dots \int_0^{2\pi} \mathcal{F}(\|x\| \cos \psi, \|x'\| \cos(\psi - \alpha)) d\psi.
\end{aligned} \tag{17}$$

This is now a product of $d-1$ one-dimensional integrals. Since $\int_0^\pi \sin^s = 0$ if s is odd, we have that the integral (17) vanishes if $i \neq j$. If instead $i = j$, we use the fact that

$$\int_0^\pi \sin^s(t) \cos^2(t) dt = \frac{(s-1)!!}{(s+2)!!} \begin{cases} \pi & \text{if } s \text{ is even} \\ 2 & \text{if } s \text{ is odd} \end{cases}$$

and we deduce that

$$\begin{aligned}
& \int_{a \in \mathbb{S}^{d-1}} a_i a_i \mathcal{F}(a \cdot x, a \cdot x') d\Omega \\
&= \eta_{d,r} \frac{(d-i+r-1)!!}{(d+r)!!} \frac{(d-i+r-2)!!}{(d-i+r+1)!!} \frac{r!!}{(d-i+r-2)!!} \int_0^{2\pi} \mathcal{F}(\|x\| \cos \psi, \|x'\| \cos(\psi - \alpha)) d\psi. \\
&= \eta_{d,r} \frac{r!!}{(d+r)!!} \int_0^{2\pi} \mathcal{F}(\|x\| \cos \psi, \|x'\| \cos(\psi - \alpha)) d\psi.
\end{aligned}$$

This proves the diagonal part in our expression for $\int aa^T \mathcal{F}(a^T x, a^T x') d\Omega$. All remaining terms as well as the two integrals $\int a \mathcal{F}(a^T x, a^T x') d\Omega$ and $\int \mathcal{F}(a^T x, a^T x') d\Omega$ follow from very similar (and slightly simpler) calculations. \square

We now apply Lemma 5 to compute the kernel K_∞ with the uniform initialization (7).

Proposition 6. *If $a \sim \mathcal{U}(\mathbb{S}^{d-1})$ and $b \sim \mathcal{U}([-k, k])$ and $\|x\|, \|x'\| < k$ then*

$$\begin{aligned}
2kV ol_{d-1}(\mathbb{S}^{d-1}) \cdot \mathbb{E}_{(a,b)}[ax+b]_+[ax'+b]_+ &= \eta_{d,0} \frac{1}{(d-2)!!} \frac{2\pi}{3} k^3 + \eta_{d,2} \frac{2}{d!!} k \|x\| \|x'\| \pi \cos(\alpha) \\
&\quad + \eta_{d,3} \frac{3}{(d+1)!!} \left([E_1]_\tau^{\tau+\pi} + [E_2]_{\tau-\pi}^\tau \right) \\
2kV ol_{d-1}(\mathbb{S}^{d-1}) \cdot \mathbb{E}_{(a,b)}[ax+b]_+ \mathbf{1}[ax'+b]_+ a &= \eta_{d,1} \frac{2}{d!!} Q^T \begin{bmatrix} 0_{d-2} \\ k\pi \|x\| \\ 0 \end{bmatrix} + \eta_{d,2} \frac{3}{(d+1)!!} Q^T \begin{bmatrix} 0_{d-2} \\ G_1 \\ G_2 \end{bmatrix} \\
2kV ol_{d-1}(\mathbb{S}^{d-1}) \cdot \mathbb{E}_{(a,b)} \mathbf{1}[ax+b] \mathbf{1}[ax'+b] aa^T &= \eta_{d,0} \frac{2\pi k}{d!!} Id_d + \eta_{d,1} \frac{3}{(d+1)!!} Q^T \begin{bmatrix} \frac{1}{3} \delta Id_{d-2} & 0 & 0 \\ 0 & \alpha & \beta \\ 0 & \beta & \gamma \end{bmatrix} Q
\end{aligned} \tag{18}$$

where $\alpha = \arccos\left(\frac{x \cdot x'}{\|x\| \|x'\|}\right)$, $\tau = \arctan\left(\frac{\|x\| - \|x'\| \cos(\alpha)}{\|x'\| \sin(\alpha)}\right)$, $Q \in SO(d)$ is such that $Qx = (0, \dots, \|x\|, 0)^T$, $Qx' = (0, \dots, \|x'\| \cos(\alpha), \|x'\| \sin(\alpha))^T$ and

$$\eta_{d,r} = \begin{cases} 2^{\lceil \frac{d-2}{2} \rceil} \pi^{\lfloor \frac{d-2}{2} \rfloor} & \text{if } r \text{ is even,} \\ 2^{\lfloor \frac{d-2}{2} \rfloor} \pi^{\lceil \frac{d-2}{2} \rceil} & \text{if } r \text{ is odd.} \end{cases}$$

$$\begin{aligned}
E_1 &= \frac{1}{18} (\sin(\psi)^3 - 3 \sin(\psi)) \|x\|^3 + \frac{1}{24} \|x\|^2 \|x'\| (3 \sin(\psi + \alpha) + \sin(3\psi - \alpha) + 6 \sin(\psi - \alpha)) \\
E_2 &= \frac{1}{18} (\sin(\psi - \alpha)^3 - 3 \sin(\psi - \alpha)) \|x'\|^3 + \frac{1}{24} \|x\| \|x'\|^2 (\sin(3\psi - 2\alpha) + 3 \sin(\psi - 2\alpha) + 6 \sin(\psi)) \\
G_1 &= \frac{1}{3} \|x\|^2 \sin(\tau)^3 - \|x\|^2 \sin(\tau) + \frac{1}{2} \|x\| \|x'\| \sin(\alpha + \tau) + \frac{1}{6} \|x\| \|x'\| \sin(-\alpha + 3\tau) \\
&\quad + \|x\| \|x'\| \sin(-\alpha + \tau) - \frac{1}{12} \|x'\|^2 \sin(-2\alpha + 3\tau) - \frac{1}{4} \|x'\|^2 \sin(-2\alpha + \tau) - \frac{1}{2} \|x'\|^2 \sin(\tau) \\
G_2 &= \frac{1}{3} \|x\|^2 \cos(\tau)^3 - \frac{1}{2} \|x\| \|x'\| \cos(\alpha + \tau) - \frac{1}{6} \|x\| \|x'\| \cos(-\alpha + 3\tau) + \frac{1}{12} \|x'\|^2 \cos(-2\alpha + 3\tau) \\
&\quad - \frac{1}{4} \|x'\|^2 \cos(-2\alpha + \tau) + \frac{1}{2} \|x'\|^2 \cos(\tau) \\
\alpha &= \left[\|x\| \sin(\psi) - \frac{1}{3} \|x\| \sin(\psi)^3 \right]_{\tau}^{\tau+\pi} + \left[\frac{1}{4} \|x'\| \sin(\alpha + \psi) + \frac{1}{12} \|x'\| \sin(3\psi - \alpha) + \frac{1}{2} \|x'\| \sin(\psi - \alpha) \right]_{\tau-\pi}^{\tau} \\
\beta &= \left[-\frac{1}{3} \|x\| \cos(\psi)^3 \right]_{\tau}^{\tau+\pi} + \left[-\frac{1}{4} \|x'\| \cos(\alpha + \psi) - \frac{1}{12} \|x'\| \cos(3\psi - \alpha) \right]_{\tau-\pi}^{\tau} \\
\gamma &= \left[\frac{1}{3} \|x\| \sin(\psi)^3 \right]_{\tau}^{\tau+\pi} + \left[-\frac{1}{4} \|x'\| \sin(\alpha + \psi) - \frac{1}{12} \|x'\| \sin(3\psi - \alpha) + \frac{1}{2} \|x'\| \sin(\psi - \alpha) \right]_{\tau-\pi}^{\tau} \\
\delta &= [\|x\| \sin(\psi)]_{\tau}^{\tau+\pi} + [\|x'\| \sin(\psi - \alpha)]_{\tau-\pi}^{\tau}
\end{aligned} \tag{19}$$

Proof. The idea is to compute the integral with respect to the bias term b and then split the result into homogeneous expressions where Lemma 5 can be applied. In particular, assuming that $-k \leq s, t \leq k$:

$$\begin{aligned}
\mathcal{I}(s, t) &= \int_{-k}^k [s+b]_+ [t+b]_+ db = \int_{\min(s, t)}^k (s+b)(t+b) db \\
&= \underbrace{\left(\frac{1}{3} k^3 \right)}_{\mathcal{I}^0} + \underbrace{\left(\frac{1}{2} k^2 (s+t) \right)}_{\mathcal{I}^1} + \underbrace{\left(kst \right)}_{\mathcal{I}^2} + \underbrace{\left(\frac{1}{3} \min(s, t)^3 - \frac{1}{2} \min(s, t)^2 (s+t) + \min(s, t) st \right)}_{\mathcal{I}^3},
\end{aligned}$$

where we collected terms that have total degree 0, 1, 2, 3 in s, t . The computation of $\int_{b \in [-k, k]} \int_{a \in \mathbb{S}^{d-1}} [ax + b]_+ [ax' + b]_+ d\Omega = \int_{a \in \mathbb{S}^{d-1}} I(a \cdot x, a \cdot x') d\Omega$ is now reduced to four one-dimensional integrals of the form $\int_0^{2\pi} \mathcal{I}^j(\|x\| \cos(\psi), \|x'\| \cos(\psi - \alpha)) d\psi$ where $\alpha = \arccos\left(\frac{x \cdot x'}{\|x\| \|x'\|}\right)$. The most tedious case is $j = 3$ where we need to compare $\|x\| \cos(\psi)$ and $\|x'\| \cos(\psi + \alpha)$. Assuming $0 \leq \alpha \leq \pi$, then $\|x\| \cos(\psi) < \|x'\| \cos(\alpha - \psi)$ holds if and only if $\tau \leq \psi \leq \tau + \pi$ where

$$\tau = \arctan\left(\frac{\|x\| - \|x'\| \cos \alpha}{\|x'\| \sin(\alpha)}\right).$$

From this we obtain that

$$\begin{aligned}
&\int_0^{2\pi} \mathcal{I}^3(\|x\| \cos(\psi), \|x'\| \cos(\alpha - \psi)) d\psi \\
&= \int_{\tau-\pi}^{\tau} \left(-\frac{1}{6} \|x'\|^3 \cos(\alpha - \psi)^3 + \frac{1}{2} \|x'\|^2 \|x\| \cos(\alpha - \psi)^2 \cos(\psi) \right) d\psi \\
&\quad + \int_{\tau}^{\tau+\pi} \left(-\frac{1}{6} \|x\|^3 \cos(\psi)^3 + \frac{1}{2} \|x\|^2 \|x'\| \cos(\psi)^2 \cos(\alpha - \psi) \right) d\psi
\end{aligned}$$

Expanding this integral we obtain the expressions for $\mathbb{E}_{(a,b)}[ax+b]_+[ax'+b]_+$ in the statement. The remaining integrals are computed similarly by considering the homogeneous parts of

$$\begin{aligned}\mathcal{I}_t(s, t) &= \int_{-k}^k [s+b]_+ \mathbf{1}[s+b] db = \int_{\min(s,t)}^k (s+b) db \\ &= \frac{1}{2} k^2 + ks + \min(s, t)s - \frac{1}{2} \min(s, t)^2\end{aligned}$$

$$\mathcal{I}_{s,t}(s, t) = \int_{-k}^k \mathbf{1}[s+b] \mathbf{1}[s+b] db = \int_{\min(s,t)}^k 1 db = k - \min(s, t).$$

□

A.2 Gaussian Initialization

The Gaussian initialization (8) yields the following simpler formula for K_∞ . The first term is well known and is derived in [10]. The second and third terms are easily derived by taking derivatives of the first term.

Proposition 7. *If $a \sim \mathcal{N}(0, Id_{d-1})$ and $b \sim \mathcal{N}(0, 1)$, then*

$$\begin{aligned}2\pi \cdot \mathbb{E}_{(a,b)}[ax+b]_+[ax'+b]_+ &= \|\tilde{x}\| \|\tilde{x}'\| (\sin(\tilde{\alpha}) + (\pi - \tilde{\alpha}) \cos(\tilde{\alpha})) \\ 2\pi \cdot \mathbb{E}_{(a,b)}[ax+b]_+ \mathbf{1}[ax'+b] a &= \|\tilde{x}\| (\sin(\tilde{\alpha}) + (\pi - \tilde{\alpha}) \cos(\tilde{\alpha})) \frac{x'}{\|\tilde{x}'\|} + (\pi - \tilde{\alpha}) \left(Id_d - \frac{x'x'^T}{\|\tilde{x}'\|^2} \right) x \\ 2\pi \cdot \mathbb{E}_{(a,b)} \mathbf{1}[ax+b] \mathbf{1}[ax'+b] aa^T &= (\pi - \tilde{\alpha}) Id + \sin(\tilde{\alpha}) \frac{x'x'^T}{\|\tilde{x}'\| \|\tilde{x}\|} \\ &\quad + \frac{1}{\sin(\tilde{\alpha})} \left(Id_d - \frac{x'x'^T}{\|\tilde{x}'\|^2} \right) \frac{xx^T}{\|\tilde{x}\| \|\tilde{x}'\|} \left(Id_d - \frac{xx^T}{\|\tilde{x}\|^2} \right),\end{aligned}\tag{20}$$

where $\tilde{x} = (x, 1)$, $\tilde{x}' = (x', 1)$, and $\tilde{\alpha} = \arccos\left(\frac{\tilde{x} \cdot \tilde{x}'}{\|\tilde{x}\| \|\tilde{x}'\|}\right)$.

B RKHS Norm of the Neural Spline Kernel

We now discuss how $c(a, b)$ in (11) is related to the Laplacian of the function. If we make the mild assumption that our functions contain a linear and bias term (Lemma 8), then $c(a, b)$ is the Radon Transform of the laplacian of the function. Thus, the least norm minimizers of the least squares problem (1) are related to the laplacian of the function and the RKHS norm corresponds to the integral of the laplacian over hyperplanes in the domain. In our experiments, we added an option to include the linear and bias terms to the solution. They appear to have no effect on the final reconstruction. The derivation below is borrowed from [24].

Lemma 8. *Let $f_{\text{lim}}(x) : \mathbb{R}^d \rightarrow \mathbb{R}$ be an infinite-width, one hidden layer neural whose weights a, b are distributed according to the measure $c(a, b) : \mathbb{S}^{d-1} \times \mathbb{R} \rightarrow \mathbb{R}$*

$$f_{\text{lim}}(x; c) = \int_{\mathbb{S}^{d-1} \times \mathbb{R}} [a^T x - b]_+ c(a, b) da db + v^T x + d. \tag{21}$$

Then, $f_{\text{lim}}(x)$ can always be rewritten as

$$\int_{\mathbb{S}^{d-1} \times \mathbb{R}} [a^T x - b]_+ c^+(a, b) da db + v'^T x + d' \tag{22}$$

where $c^+(a, b)$ is an even measure on $\mathbb{S}^{d-1} \times \mathbb{R}$, $v \in \mathbb{R}^d$, and $d \in \mathbb{R}$.

Proof. We can split the integral in f_{lim} into even and odd parts:

$$\begin{aligned}f_{\text{lim}}(x) &= \frac{1}{2} \int_{\mathbb{S}^{d-1} \times \mathbb{R}} ([a^T x - b]_+ + [a^T x - b]_-) c^+(a, b) da db \\ &\quad + \frac{1}{2} \int_{\mathbb{S}^{d-1} \times \mathbb{R}} ([a^T x - b]_+ - [a^T x - b]_-) c^-(a, b) da db \\ &\quad + v^T x + d\end{aligned}$$

where c^+ and c^- are the even and odd parts of c respectively. Observing that $[t]_+ + [-t]_+ = |t|$ and $[t]_+ - [-t]_+ = t$, we have that

$$f_{\text{lim}}(x) = \frac{1}{2} \int_{\mathbb{S}^{d-1} \times \mathbb{R}} (|a^T x - b| c^+(a, b) + (a^T x - b) c^-(a, b)) da db + v^T x + d \quad (23)$$

$$= \frac{1}{2} \int_{\mathbb{S}^{d-1} \times \mathbb{R}} |a^T x - b| c^+(a, b) da db + v'^T x + d' \quad (24)$$

$$= \int_{\mathbb{S}^{d-1} \times \mathbb{R}} [a^T x - b]_+ c^+(a, b) da db + v'^T x + d' \quad (25)$$

where $v' = v + \int_{\mathbb{S}^{d-1} \times \mathbb{R}} a c^-(a, b) da db$, $d' = d + \int_{\mathbb{S}^{d-1} \times \mathbb{R}} b c^-(a, b) da db$, and the last step holds because c^+ is even. \square

Using Lemma 8, we will consider without loss of generality, neural networks of the form (21) with even measures $c(a, b)$. We now give a few useful definitions and lemmas.

Definition 9. Let $f : \mathbb{R}^d \rightarrow \mathbb{R}$. The *Radon Transform* of f is

$$\mathcal{R}\{f\}(a, b) := \int_{a^T x = b} f(x) ds(x) \quad (26)$$

where $ds(x)$ is a measure on the $(d-1)$ -hyperplane $a^T x = b$. Intuitively the Radon transform represents a function in terms of its integrals along all possible hyperplanes.

Remark 10. Since the hyperplane $a^T x = b$ is the same as the hyperplane $-a^T x = -b$, the Radon transform is an even function. i.e. $\mathcal{R}\{f\}(a, b) = \mathcal{R}\{f\}(-a, -b)$.

Definition 11. Let $\varphi : \mathbb{S}^{d-1} \times \mathbb{R} \rightarrow \mathbb{R}$. The *Dual Radon Transform* of φ is the adjoint of the Radon Transform \mathcal{R}

$$\mathcal{R}^*\{\varphi\}(x) := \int_{\mathbb{S}^{d-1}} \varphi(a, x^T a) d\Omega \quad (27)$$

where $d\Omega$ is a measure on the $(d-1)$ -hypersphere \mathbb{S}^{d-1} . Intuitively the Dual Radon transform represents a function at x in terms of its integrals on all hyperplanes through x .

The Radon Transform satisfies the *intertwining property*. i.e. for any positive integer s

$$\mathcal{R}\{(-\Delta)^{\frac{s}{2}} f\} = (-\partial_b^2)^{\frac{s}{2}} \mathcal{R}\{f\} \quad (28)$$

Lemma 12. (Solmon [28]) If $\varphi(a, b) = \varphi(-a, -b)$ is an even function mapping $\mathbb{S}^{d-1} \times \mathbb{R}$ to \mathbb{R} which is C^∞ smooth and whose partial derivatives decrease at a rate faster than $\mathcal{O}(|b|^{-N})$ as $|b| \rightarrow \infty$ for any $N \geq 0$, then the Dual Radon Transform can be inverted using

$$\frac{1}{2(2\pi)^{d-1}} \mathcal{R}\{(-\Delta)^{\frac{d-1}{2}} \mathcal{R}^*\{\varphi\}\} = \varphi \quad (29)$$

Lemma 13. (Ongie et al. [24]) Let $f_{\text{lim}}(x) : \mathbb{R}^d \rightarrow \mathbb{R}$ be an infinite-width, one hidden layer neural whose weights a, b are distributed according to the even measure $c(a, b)$. Then $c(a, b)$ can be expressed as

$$c(a, b) = \gamma_d \mathcal{R}\{(-\Delta)^{\frac{d+1}{2}} f_{\text{lim}}(x)\},$$

where $\mathcal{R}\{f\}(a, b)$ is the Radon Transform of f . In particular, for $d = 3$,

$$\gamma_d \mathcal{R}\{\Delta f_{\text{lim}}(x)\} = c(a, b)$$

Proof. The Laplacian of f_{lim} in is (21)

$$\Delta f_{\text{lim}}(x; c) = \int_{\mathbb{S}^{d-1} \times \mathbb{R}} \delta(a^T x - b) c(a, b) da db = \int_{\mathbb{S}^{d-1}} c(a, a^T x) d\Omega \quad (30)$$

which is precisely the Dual Radon Transform of $c(a, b)$. Since c is even, and assuming it decays rapidly with b , we can invert it using Lemma 12 yielding

$$c(a, b) = \gamma_d \mathcal{R}\{(-\Delta)^{\frac{d+1}{2}} f_{\text{lim}}(x)\}.$$

\square

Corollary 14. The RKHS norm of the function f_{lim} is

$$\|f_{\text{lim}}\|_{\mathcal{H}} = \|c(a, b)\|_2 + \|v\|_2 + |d| = \left(\int_{\mathbb{S}^{d-1} \times [-k, k]} c(a, b)^2 d\Omega db \right)^{\frac{1}{2}} + \|v\|_2 + |d| \quad (31)$$

C Poisson Surface Reconstruction Kernel

In its simplest form, Poisson reconstruction of a surface [20], extracts the level set of a smoothed indicator function determined as the solution of

$$-\Delta f = \nabla \cdot V,$$

where V is a vector field obtained from normals n_i at samples x_i , and we use f to denote the (smoothed) indicator function as it plays the same role as f in (1). The equation above is closely related to (1): specifically, it is the equation for the minimizer of $\int_{\mathbb{R}^3} \|\nabla_x f(x) - V\|^2 dx$, i.e., the second term in (1), can be viewed as a approximation of this term by sampling at x_i . The screened form of Poisson reconstruction effectively adds the first term with $y_i = 0$, as the indicator function at points of interest is supposed to be zero. For the Poisson equation, the solution can be explicitly written as an integral

$$f(x) = \int_{\mathbb{R}^3} \frac{\nabla_z \cdot V(z) dz}{|x - z|}$$

The vector field V is obtained by interpolating the normals using a fixed-grid spline basis and barycentric coordinates of the sample points with respect to the grid cell containing it. This is equivalent to using a non-translation invariant non-symmetric locally-supported kernel $K_B(z, x)$:

$$V(z) = \sum_i K_B(z, x_i) n_i.$$

Let $B_{1,3}(x - c_j)$, $x \in \mathbb{R}^3$ be the trilinear basis $B_1(x^1 - c_j^1)B_1(x^2 - c_j^2)B_1(x^3 - c_j^3)$ function centered at a regular grid point c_j , and $B_{n,3}(x - c_j)$ be a tensor-product spline basis function of degree n defined in a similar way. (Note that in Lemma 3 in the main document, we slightly abuse notation, denoting B_1 as the trilinear basis and B_n as the degree- n spline basis). Poisson reconstruction uses $n = 1$ or $n = 2$ where

$$B_2(x) = \begin{cases} 0 & \text{if } x < -1.5 \\ \frac{1}{2}x^2 & \text{if } -1.5 \leq x < -0.5 \\ -\frac{1}{2} + x - (x-1)^2 & \text{if } -0.5 \leq x < 0.5 \\ \frac{5}{2} - x + \frac{1}{2}(x-2)^2 & \text{if } 0.5 \leq x < 1.5 \\ 0 & \text{if } 1.5 \leq x \end{cases} \quad (32)$$

Then $K_B(z, x) = \sum_j B_{1,3}(x - c_j)B_{n,3}(z - c_j)$, where only 8 terms corresponding to the vertices c_j of the grid cube containing x are nonzero. This yields the following expression for the kernel corresponding to Poisson reconstruction,

$$K_{\text{PR}}(x, x')_g = \int_{\mathbb{R}^3} \frac{\nabla_z K_B(z, x') dz}{|x - z|}$$

i.e., the convolution of the Laplacian kernel $1/|x - z|$ and the gradient of K_B . Using the identity $\nabla(f * g) = (\nabla f * g)$, we can write this as the gradient of $K_{\text{PR}}(x, x')_g$, defined as

$$K_{\text{PR}}(x, x') = \int_{\mathbb{R}^3} \frac{K_B(z, x') dz}{|x - z|} \quad (33)$$

To make it easier to understand the qualitative behavior of the kernel, replacing $K_B(z, x)$ with a radial kernel $B_n^1(|z - x|)$, with qualitatively similar behavior (see Figure 4) yields a translation-invariant radial approximation $K_{\text{PR}}^{\text{approx}}$ of the kernel K_{PR} , as the convolution of two radial kernels is a radial function.

$$K^{\text{approx}}(x, x') = \int_{\mathbb{R}^3} \frac{B_n^1(|z - x'|) dz}{|x - z|} \quad (34)$$

As both B_n^1 and the Laplace kernel are radial functions, their convolution is also radial. It can be expressed in a more explicit form using the relation between Fourier and Hankel transforms for radial functions. For $n = 3$, the Hankel transform is related to Fourier transform by [26]

$$s^{1/2} \mathcal{F}[g](s) = (2\pi)^{3/2} \mathcal{H}[g](s)$$

The Hankel transform is an involution, so the relationship for the inverse Fourier transform is similar. Writing $g * h = \mathcal{F}^{-1}[\mathcal{F}[g]\mathcal{F}[h]]$, we obtain the expression for the radial convolution in terms of one-dimensional integrals,

$$K^{\text{approx}}(x) = \mathcal{H}_s[s^{-3/2}\mathcal{H}_r[B_n^1]](|x|),$$

where we use $\mathcal{H}_r[1/r] = 1/s$. and $K_g^{\text{approx}}(x)$ is just the gradient of this, i.e., a derivative times $|x|/x$. The RKHS norm for the space corresponding to this kernel is given by

$$\|f\|_{\mathcal{H}} = \int \frac{|\mathcal{F}[f]|^2}{\mathcal{F}[K^{\text{approx}}]} d\omega$$

with $\mathcal{F}[K^{\text{approx}}]$ obtained using the Hankel transforms as above.

D Additional Experiments

D.1 Quantitative Results Per ShapeNet Class

Tables 2 and 3 below show the per ShapeNet category IoU and Chamfer distance statistics for the benchmark described in Section 4.1.

Class	Poisson			Eikonal			Neural Spline		
	mean	median	std	mean	median	std	mean	median	std
car	0.6637	0.7192	0.1255	0.8102	0.8459	0.1236	0.9082	0.9399	0.0747
chair	0.5880	0.6046	0.1243	0.8216	0.8654	0.1139	0.9056	0.9369	0.1062
airplane	0.5954	0.6139	0.0581	0.7804	0.8161	0.0913	0.7773	0.8796	0.1961
display	0.7027	0.7072	0.0800	0.8673	0.8990	0.0690	0.9533	0.9549	0.0188
table	0.3720	0.3565	0.1334	0.7747	0.7772	0.0742	0.8968	0.9011	0.0500
rifle	0.6803	0.6791	0.0532	0.8381	0.8479	0.0568	0.9489	0.9491	0.0169
cabinet	0.7301	0.7764	0.1095	0.8853	0.8916	0.0782	0.9478	0.9467	0.0377
loudspeaker	0.7432	0.7848	0.1309	0.8595	0.9452	0.2038	0.9507	0.9768	0.0518
telephone	0.7883	0.7990	0.0552	0.9148	0.9372	0.0639	0.9746	0.9772	0.0202
bench	0.4728	0.4384	0.1213	0.5862	0.6394	0.2486	0.8160	0.8900	0.1365
sofa	0.7122	0.7326	0.0662	0.8870	0.9210	0.1211	0.9565	0.9644	0.0267
watercraft	0.6523	0.6793	0.0994	0.8272	0.8537	0.0845	0.9340	0.9380	0.0462
lamp	0.5413	0.5786	0.1858	0.8251	0.8352	0.1093	0.9467	0.9470	0.0306
All Classes:	0.6340	0.6728	0.1577	0.8213	0.8566	0.1461	0.9167	0.9438	0.0985

Table 2: Quantitative comparison of the Intersection over Union (IoU) Distance between Neural Splines and Poisson Surface Reconstruction over a subset (20 models per class) of the ShapeNet dataset. For the Poisson results, we selected the best reconstruction over a sweep of input parameters.

Class	Poisson			Eikonal			Neural Spline		
	mean	median	std	mean	median	std	mean	median	std
car	2.27e-4	2.22e-4	8.04e-5	2.60e-4	2.82e-4	9.80e-5	8.21e-5	7.23e-5	3.59e-5
chair	2.82e-4	2.13e-4	1.84e-4	9.25e-4	9.88e-5	3.11e-3	5.52e-5	4.20e-5	4.01e-5
airplane	8.37e-5	8.76e-5	1.77e-5	3.04e-4	1.74e-4	3.47e-4	3.55e-5	3.45e-5	2.45e-6
display	2.45e-4	2.13e-4	1.11e-4	9.99e-5	7.49e-5	8.44e-5	4.31e-5	3.95e-5	1.24e-5
table	3.50e-4	2.53e-4	2.14e-4	3.40e-4	1.95e-4	3.33e-4	6.44e-5	4.78e-5	4.01e-5
rifle	4.46e-5	3.11e-5	2.76e-5	9.62e-5	5.29e-5	1.25e-4	3.27e-5	3.16e-5	2.81e-6
cabinet	3.62e-4	2.91e-4	1.96e-4	1.56e-4	9.39e-5	1.23e-4	6.93e-5	4.67e-5	4.30e-5
loudspeaker	4.29e-4	3.54e-4	2.68e-4	3.77e-3	1.15e-4	1.49e-2	8.27e-5	4.58e-5	7.24e-5
telephone	1.28e-4	1.17e-4	3.36e-5	1.03e-4	4.43e-5	1.54e-4	3.33e-5	3.18e-5	3.42e-6
bench	1.93e-4	1.93e-4	8.14e-5	4.48e-4	2.58e-4	4.33e-4	5.62e-5	4.74e-5	2.05e-5
sofa	2.72e-4	2.46e-4	1.02e-4	2.86e-4	1.02e-4	5.30e-4	5.08e-5	4.81e-5	1.22e-5
watercraft	1.07e-4	8.82e-5	6.12e-5	1.47e-4	1.12e-4	1.23e-4	4.41e-5	3.84e-5	1.42e-5
lamp	1.61e-4	1.35e-4	1.02e-4	1.72e-3	1.28e-4	6.24e-3	4.15e-5	3.89e-5	9.61e-6
All Classes:	2.22e-4	1.70e-4	1.76e-4	6.66e-4	1.07e-4	4.69e-3	5.32e-5	4.07e-5	3.53e-5

Table 3: Quantitative comparison of the Chamfer Distance between Neural Splines and Poisson Surface Reconstruction over a subset (20 models per class) of the ShapeNet dataset. For the Poisson results, we selected the best reconstruction over a sweep of input parameters.

D.2 Empirical versus Analytical Kernel

Figure 9 compares results using the empirical kernel with m neurons and using the analytical kernel. Figure 8 shows the convergence of the empirical Kernel to the analytic one as the number m of neurons grows.

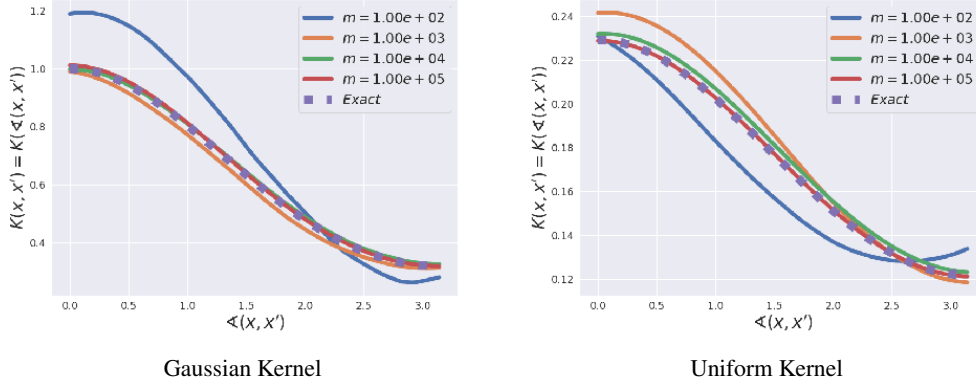


Figure 8: Convergence of the empirical kernels to the exact ones. Both the Gaussian (left) and Uniform (right) kernels are rotation invariant and thus depend only on the angle $\angle(x, x')$ between x and x' . This plot shows the value of the kernel as a function of this angle from 0 to π (we show here only the scalar term of the kernel $\mathbb{E}_{(a,b)}[ax + b]_+[ax' + b]_+$).

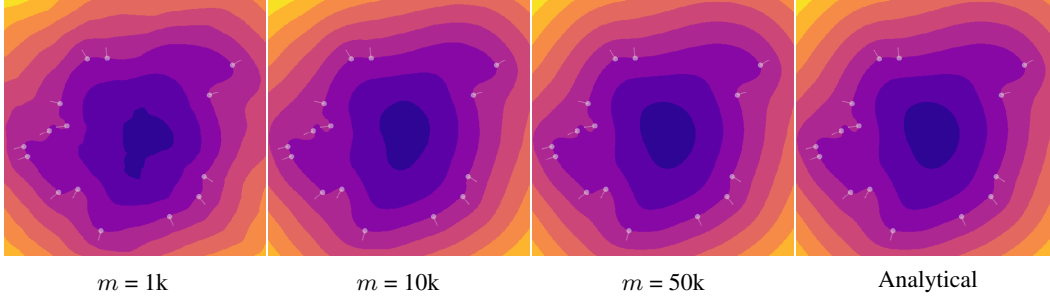


Figure 9: The effect of using an approximate kernel with m neurons to do reconstruction. Increasing m makes the approximation closer to the analytical version.

D.3 Quantitative Comparison between Gaussian and Uniform Kernels

Tables 4 and 5 below show a quantitative comparison between Neural Splines using the Gaussian initialization (8) and the Uniform initialization (7) on the benchmark described in Section (4.1). The results in both cases are very close to each other in both Chamfer distance and in IoU.

Class	Neural Spline (Uniform)			Neural Spline (Gaussian)		
	mean	median	std	mean	median	std
car	0.9082	0.9399	0.0747	0.9084	0.9392	0.0743
chair	0.9056	0.9369	0.1062	0.9131	0.9357	0.0852
airplane	0.7773	0.8796	0.1961	0.8388	0.9159	0.1531
display	0.9533	0.9549	0.0188	0.9523	0.9535	0.0193
table	0.8968	0.9011	0.0500	0.8952	0.8980	0.0508
rifle	0.9489	0.9491	0.0169	0.9488	0.9498	0.0185
cabinet	0.9478	0.9467	0.0377	0.9477	0.9475	0.0377
loudspeaker	0.9507	0.9768	0.0518	0.9500	0.9768	0.0531
telephone	0.9746	0.9772	0.0202	0.9741	0.9774	0.0209
bench	0.8160	0.8900	0.1365	0.8195	0.8902	0.1296
sofa	0.9565	0.9644	0.0267	0.9584	0.9643	0.0221
watercraft	0.9340	0.9380	0.0462	0.9360	0.9386	0.0404
lamp	0.9467	0.9470	0.0306	0.9457	0.9459	0.0319
All Classes:	0.9167	0.9438	0.0985	0.9221	0.9441	0.0834

Table 4: Comparison of IoU between Gaussian and Uniform kernels on the benchmark described in Section 4.1.

Class	Neural Spline (Uniform)			Neural Spline (Gaussian)		
	mean	median	std	mean	median	std
car	8.21e-05	7.23e-05	3.59e-05	8.21e-05	7.18e-05	3.60e-05
chair	5.52e-05	4.20e-05	4.01e-05	5.62e-05	4.21e-05	4.32e-05
airplane	3.55e-05	3.45e-05	2.45e-06	3.55e-05	3.44e-05	2.45e-06
display	4.31e-05	3.95e-05	1.24e-05	4.36e-05	3.99e-05	1.28e-05
table	6.44e-05	4.78e-05	4.01e-05	6.60e-05	4.88e-05	4.17e-05
rifle	3.27e-05	3.16e-05	2.81e-06	3.26e-05	3.15e-05	2.79e-06
cabinet	6.93e-05	4.67e-05	4.30e-05	6.98e-05	4.69e-05	4.34e-05
loudspeaker	8.27e-05	4.58e-05	7.24e-05	8.41e-05	4.54e-05	7.54e-05
telephone	3.33e-05	3.18e-05	3.42e-06	3.34e-05	3.19e-05	3.60e-06
bench	5.62e-05	4.74e-05	2.05e-05	5.66e-05	4.82e-05	2.09e-05
sofa	5.08e-05	4.81e-05	1.22e-05	5.11e-05	4.80e-05	1.24e-05
watercraft	4.41e-05	3.84e-05	1.42e-05	4.41e-05	3.84e-05	1.42e-05
lamp	4.15e-05	3.89e-05	9.61e-06	4.19e-05	3.91e-05	1.00e-05
All Classes:	5.32e-05	4.07e-05	3.53e-05	5.36e-05	4.06e-05	3.64e-05

Table 5: Comparison of Chamfer Distance between Gaussian and Uniform kernels on the benchmark described in Section 4.1.

D.4 Figures from each ShapeNet Category

Below we show at least one model reconstructed from each ShapeNet category. The models are reconstructed using Neural Splines, Screened Poisson Surface Reconstruction [20] and Eikonal Reconstruction [13] as described in Section 4.1.

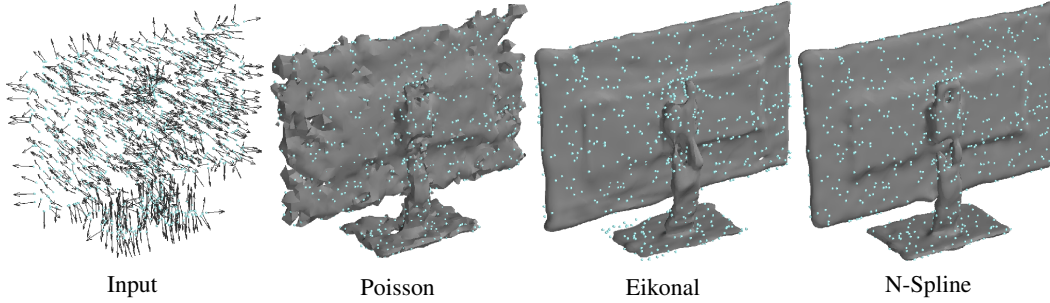


Figure 10: Comparisons between reconstruction techniques.

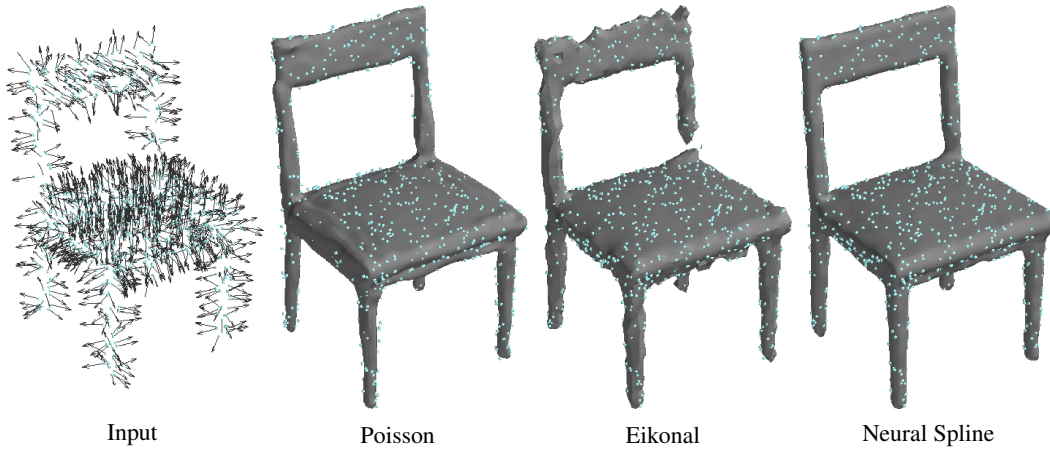


Figure 11: Comparisons between reconstruction techniques.

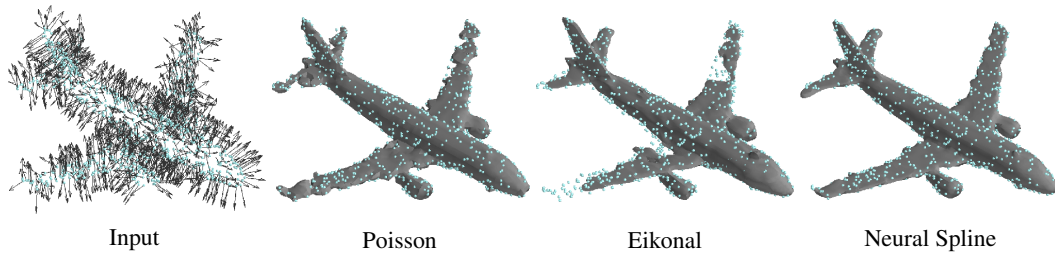


Figure 12: Comparisons between reconstruction techniques.

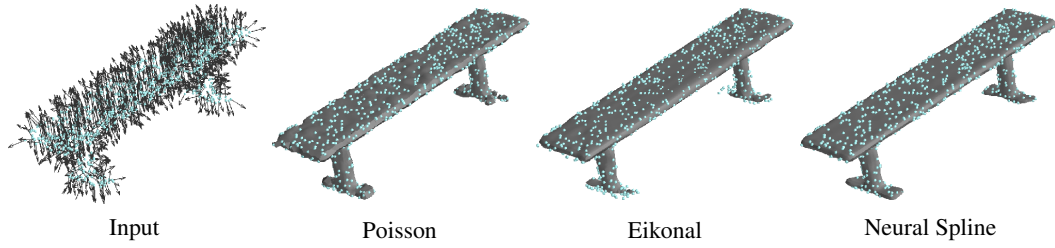


Figure 13: Comparisons between reconstruction techniques.

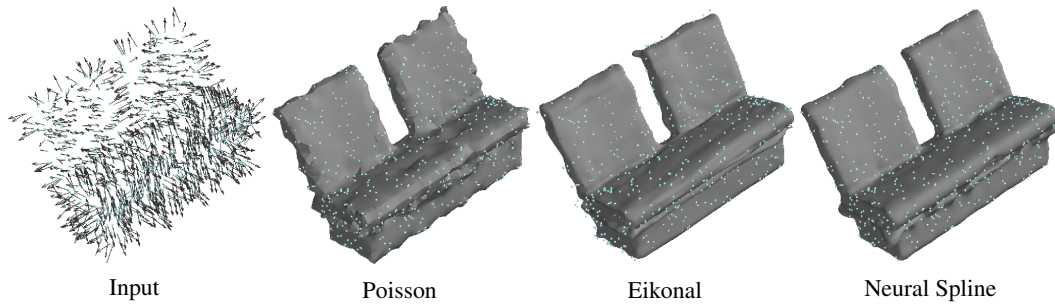


Figure 14: Comparisons between reconstruction techniques.

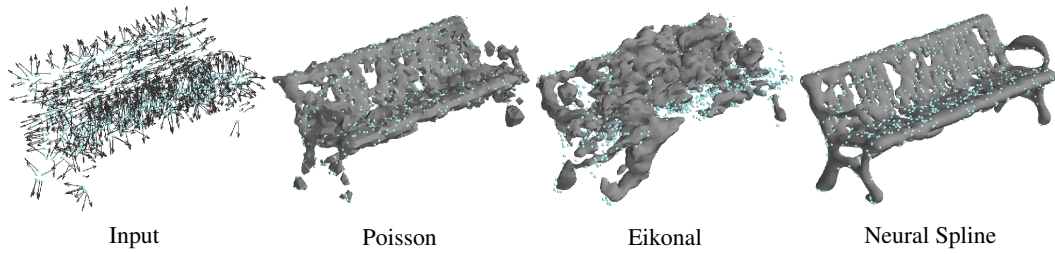


Figure 15: Comparisons between reconstruction techniques.

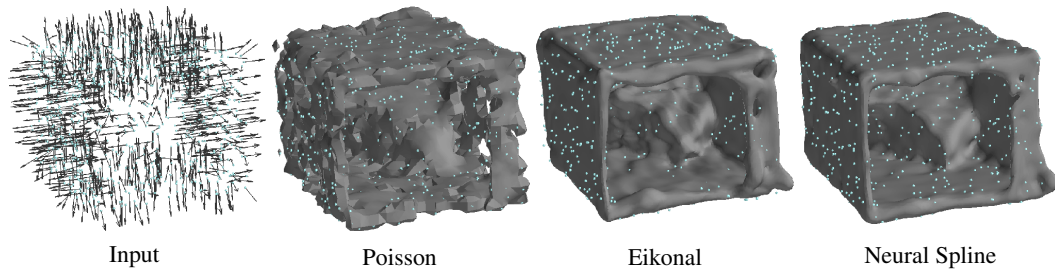


Figure 16: Comparisons between reconstruction techniques.

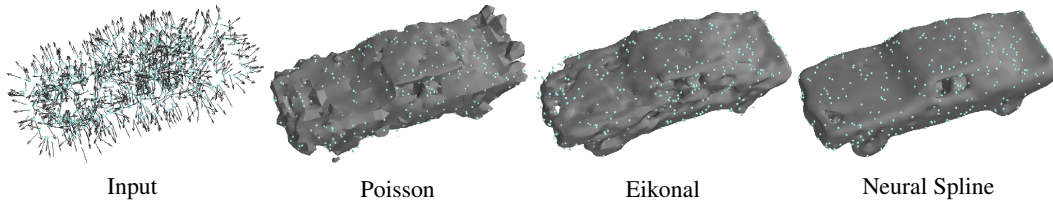


Figure 17: Comparisons between reconstruction techniques.

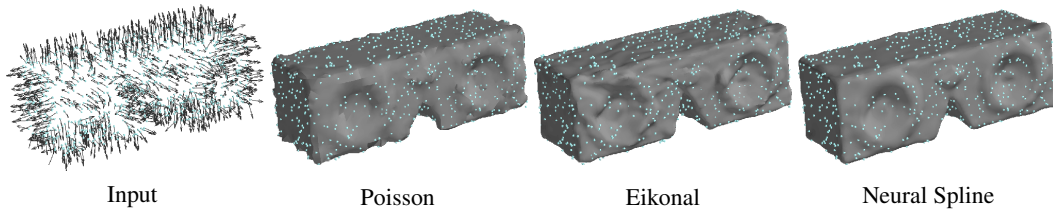


Figure 18: Comparisons between reconstruction techniques.

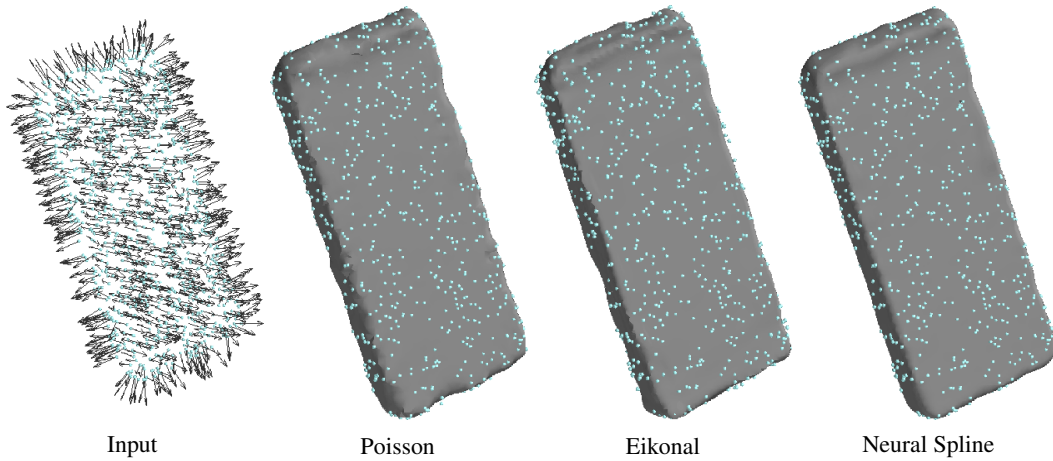


Figure 19: Comparisons between reconstruction techniques.

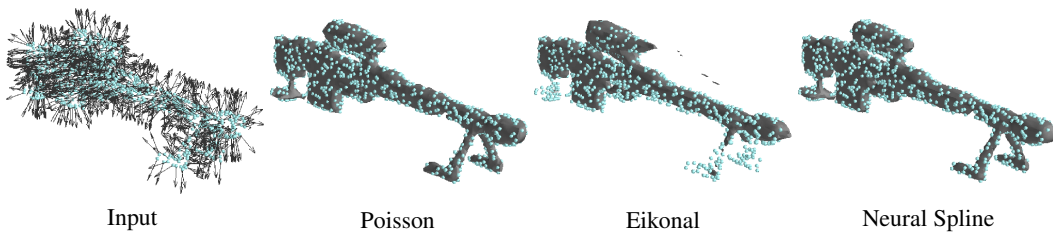


Figure 20: Comparisons between reconstruction techniques.

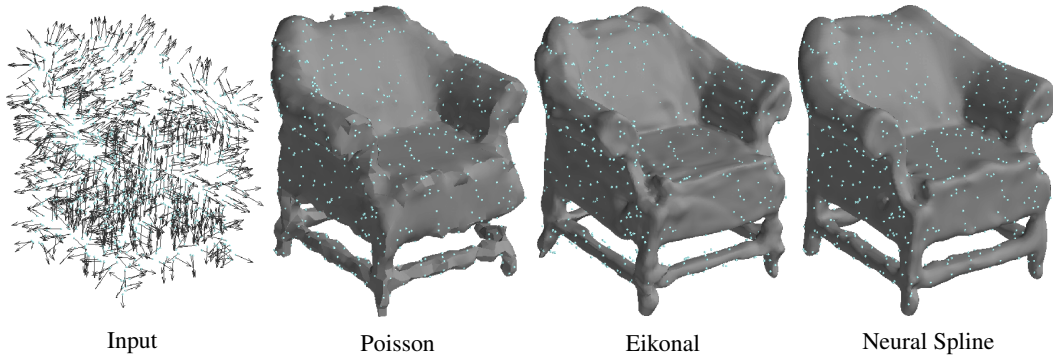


Figure 21: Comparisons between reconstruction techniques.

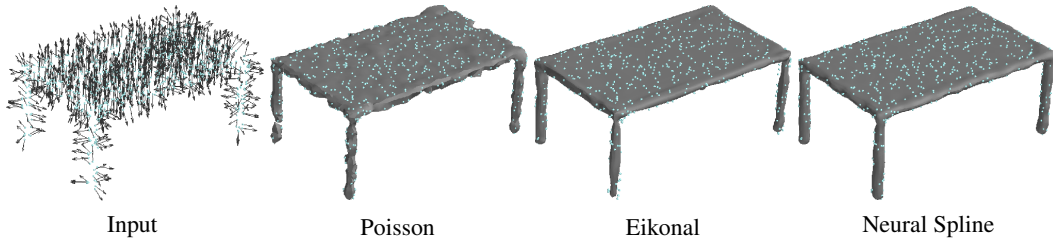


Figure 22: Comparisons between reconstruction techniques.

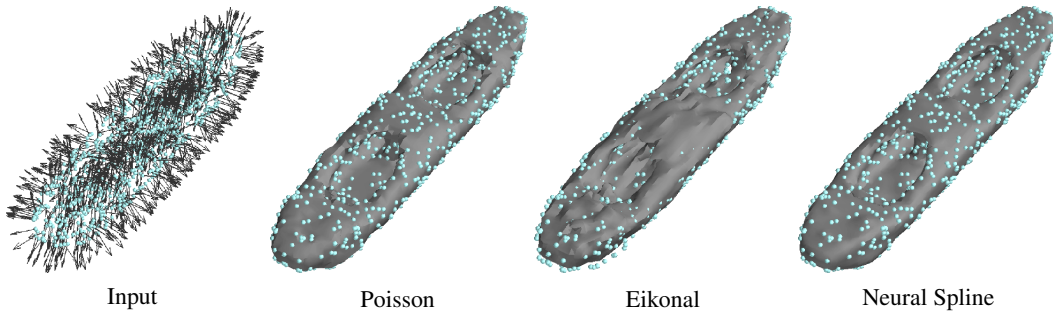


Figure 23: Comparisons between reconstruction techniques.

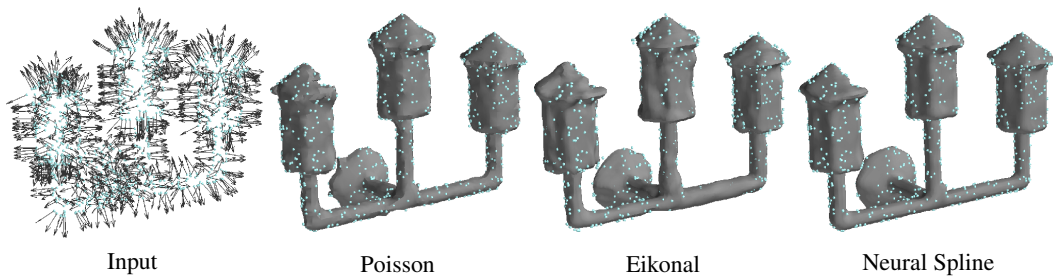


Figure 24: Comparisons between reconstruction techniques.